JMEPEG
https://doi.org/10.1007/s11665-024-09671-5

1059-9495/$19.00

ORIGINAL RESEARCH ARTICLE

Corrosion Behavior of Fluorine-Doped Calcium Phosphorus Coating on AZ31 Alloy with Various Chemical Conversion Parameters

Liuwei Zheng, Lifei Wang, Hua Chai, Chaoyang Yang, Qiuyan Huang, Zhipeng Ge, Hongxia Wang, Weili Cheng, Hua Zhang, Fugang Qi, Xiaoye Zhou, Hanuma Reddy Tiyyagura, and Kwang Seon Shin

Submitted: 23 September 2023 / Revised: 16 May 2024 / Accepted: 18 May 2024

To improve the corrosion resistance of biomedical magnesium alloys, fluoride ions (0.3 M, 0.5 M, and 0.7 M) were added to a solution of water containing 0.042 mol/L $Ca(NO_3)_2{\cdot}4H_2O$ and 0.025 mol/L $NH_4H_2PO_4$. Calcium Phosphorus (Ca-Ph) coatings with different morphology and corrosion resistance were obtained by changing the temperature and fluorine ion content to explore the growth mechanism of fluorine-doped Calcium Phosphorus (F-CaP) coating. The surface morphologies, and chemical compositions of these coatings were characterized by x-ray diffraction, scanning electron microscopy and energy-dispersive spectroscopy, and the corrosion resistances of the coatings were investigated by electrochemical tests and immersion tests. The results show that temperature has a great effect on the morphology of F-CaP coating. An increase in the temperature accelerated the reaction rate of the ions during the deposition process, and the low amount of fluoride prevented the F-CaP coating from fully covering the surface of the matrix. When the amount of doped fluorine was 0.5 M at 60 °C, the complete and compact coating morphology effectively protected the AZ31 magnesium alloy from the corrosion of simulated body fluids.

Keywords coating, corrosion behavior, magnesium

1. Introduction

Mg and its alloys are becoming increasingly popular owing to their outstanding biological compatibility, suitable mechanical properties, and special biodegradable properties (Ref 1-4). However, the low corrosive resistance of Mg alloys leads to degradation while H_2 gas is produced during this process, which can cause severe problems in the surrounding tissues (Ref 5, 6).

Liuwei Zheng, Lifei Wang, Hua Chai, Chaoyang Yang, Zhipeng Ge, Hongxia Wang, and **Weili Cheng**, College of Materials Science and Engineering, Taiyuan University of Technology, Taiyuan 030024, People's Republic of China; **Qiuyan Huang**, Institute of Metal Research, Chinese Academy of Sciences, Shenyang 110016, People's Republic of China; **Hua Zhang**, Institute for Advanced Studies in Precision Materials, Yantai University, Yantai 264005, People's Republic of China; **Fugang Qi**, School of Materials Science and Engineering, Xiangtan University, Xiangtan 411105, People's Republic of China; **Xiaoye Zhou**, Department of Materials Science and Engineering, Shenzhen MSU-BIT University, Shenzhen 518172, People's Republic of China; **Hanuma Reddy Tiyyagura**, Rudolfovo-Science and Technology Centre Novo Mesto, Podbreznik 15, 8000 Novo Mesto, Slovenia; and **Kwang Seon Shin**, Research Institute of Advanced Materials, Department of Materials Science and Engineering, Seoul National University, Gwanak-ro, Gwanak-gu, Seoul 08826, Republic of Korea. Contact e-mail: wanglifei@tyut.edu.cn.

The use of calcium phosphorus coatings is a promising method for enhancing the resistance of Mg to corrosion (Ref 7, 8), and the addition of fluoride ions benefits human bone growth and regeneration, as well as the crystallinity index (Ref 9, 10). Moreover, the introduction of fluorine can further reduce the solubility of hydroxyapatite (HA) while maintaining its biocompatibility (Ref 11, 12). H.R. Bakhsheshi-Rad et al. (Ref 13) prepared HA on Mg alloys by conventional galvanostatic electrode position, which showed improved corrosion resistance compared with that of the HA film alone. Moreno et al. (Ref 14) reported that a fluoro-doped treatment of hydroxyapatite would result in fluoro-doped hydroxyapatite with a solubility reduction of approximately 5 orders of magnitude. Moreover, fluorine-doped hydroxyapatite is considered to have good mineralization properties and the ability to promote cell proliferation (Ref 15).

Based on the above ideas, in this study, fluoride ions were introduced into a Ca-Ph treatment solution, the morphology and composition of the coating at different temperatures and fluoride contents were compared and analyzed, and the corrosion resistance of the F-CaP coating prepared by chemical conversion under the preferred process was studied through immersion and electrochemical experiments.

2. Experiments

2.1 Materials Preparation

Commercial AZ31 Mg alloys were cut into small pieces measuring 15 × 15 × 1 mm in size. These small pieces were polished gradually with sandpaper at grades #600, #800, #1000, and #1200. Then the pieces were dried after being

Published online: 03 June 2024

ultrasonically cleared with alcohol and distilled water. To explore the influence of fluoride ions on the resistance to corrosion and composition of coatings, samples were deposited on AZ31 in the bath that contained the solution of 0.042 mol/L Ca (NO3)24H2O and 0.025 mol/L NH4H2PO4. The temperature was changed from 40 to 80 °C, and the fluoride ion concentration was increased from 0.3 to 0.7 M. The samples were then removed from the solution, thoroughly rinsed, and allowed to dry naturally at ambient temperature before being used for specimen characterization, electrochemical measurements, and immersion testing.

2.2 Surface Characterization

Scanning electron microscopy (SEM; Mira 3XMU) and energy-dispersive spectroscopy (EDS) were used to determine the surface morphologies and elemental compositions of these coatings. x-ray diffraction (XRD; SmartLsb SE03030502) was used to analyze the crystal structure of the coating layer using Cu-K radiation (λ = 1.54184 nm) at a scanning speed of 5° per min in the range of 20°− 80°.

2.3 Electrochemical Tests

Electrochemical experiments were carried out in a standard three electrode system on a CHI660 electrochemical working station with a counter electrode composed of platinum. The working electrode was the specimen, and the reference electrode was an Ag/AgCl electrode. The open circuit potential (OCP) of the fluoride-coated specimens was measured for half an hour to regulate the solution and achieve equilibrium. After OCP, electrochemical impedance spectroscopy (EIS) measurements were performed in the frequency range from 0.1 to 100 kHz, and the data were analyzed using Zsimp Win software (Ref 16). Potentiodynamic polarization (PDP) experiments were performed after the EIS test. According to ASTM standard G 102-89, the electrochemical corrosion characteristics (such as the corrosion rate, current density, and corrosion potential) were calculated using a Tafel plot (Ref 17). Simulated body fluid (SBF) was used as an electrolyte to simulate human body fluid conditions (Ref 18). Each treatment condition, as well as the untreated samples, received three measurements.

2.4 Immersion Test

To evaluate the corrosion resistance of the coated samples, immersion experiments in SBF at a pH of 7.4 were performed. For this test. The coated samples with a surface area of 2.25 cm^2 were submerged in SBF and soaked at 37 °C for 7 days. To maintain the ion concentration, the solution was refreshed every two days. After 7 days, these samples were removed from the SBF and dried at ambient temperature. The ability to resist corrosion was assessed by integrating hydrogen evolution with sample weight loss during the test.

3. Results and Discussion

3.1 F-CaP Coating Characterization at Different Temperatures

Figure 1 shows the surface morphology of the F-CaP coated samples prepared at various temperatures, and the related EDS results are shown in Figure 1(d). It is obviously true that temperature has a significant impact on micromorphology. The surface morphology of the samples prepared at 40 °C is shown in Figure 1(a). The surface of the sample is similar to a dry riverbed with a certain amount of cracks, and such a structure does not easily to resist the invasion of corrosive substances. When the treatment temperature approaches 60 °C, the petal-like structure of a single compact scale-like crystal covers the surface of the matrix, and there are no obvious holes in the film layer, which can be attributed to the increasing temperature accelerating the pace of the ion reaction during the conversion procedure, resulting in a compact coating (Ref 19). The compact and intact coating showed good resistance to erosion in subsequent immersion tests. When the treatment temperature reaches 80 °C, the reaction accelerates, and a large number of bubbles are sharply generated. The morphology of the coating changes from a relatively regular stacking scaly structure to an irregular rod and needle-like agglomeration structure, and the existence of micropores and microcracks on the surface (Ref 20). On the one hand, these bubbles will occupy the space of the crystal growth, so that some positions cannot be coated by the coating. On the other hand, these bubbles will produce an impact force when they rupture, which may cause the formed coating to fall off and dissolve. During the commissioning of the samples, these pores may become channels for corrosive substances through the coating. The EDS results show that the contents of Mg and Al in the sample are very low, indicating that the coating prepared under all conditions could effectively cover the surface of the substrate. A higher fluorine content was tested, proving that fluorine was successfully doped in the Ca-Ph coating (Ref 21). Figure 1(e) shows that the Ca/P ratio increases with increasing temperature to 1.63 at 80 °C, which is close to the standard stoichiometry of HA (1.67) and explains the appearance of the typical needle HA and FHA peaks in the XRD pattern shown in Figure 2. This proves the successful preparation of FHA on the surface of the AZ31 magnesium alloy, while the Ca/P ratio was 1.4 at 60 °C, indicating that DCPD was deposited at lower temperatures.

3.2 Characterization of F-CaP Coatings Synthesized with Different Fluoride Additions

The micromorphology of the F-CaP coatings prepared with different fluoride additions at 60 °C is shown in Figure 3. When the amount of NaF was 0.3 M, the coating was composed of leaf-like crystals. However, obvious holes are visible due to insufficient F-CaP coating formation to cover the matrix surface. With increasing fluorine addition, the crystal size decreases, which could be caused by the replacement of the original OH^- of fluorine-doped hydroxyapatite by fluorine atoms, and the fluorine atoms are less abundant than OH^-, so the hydroxyapatite crystal size decreases after replacement (Ref 22, 23). When the amount of fluoride ions added reached 0.5 M, the coating was uniformly and densely arranged on the surface of the matrix. Figure 3(c) clearly shows the coating prepared by adding 0.7 M fluorine, and large cracks appear in the underlying coating. Therefore, it can be concluded that the amount of fluoride ions introduced has a considerable influence on the ability of the F-CaP coating to resist corrosion. The doping of fluorine ions not only changes the morphology of the hydroxyapatite coating but also reduces the calcium and phosphorus density of the coating when fluorine ions are present in excess. This can be attributed to the fact that F and Cl

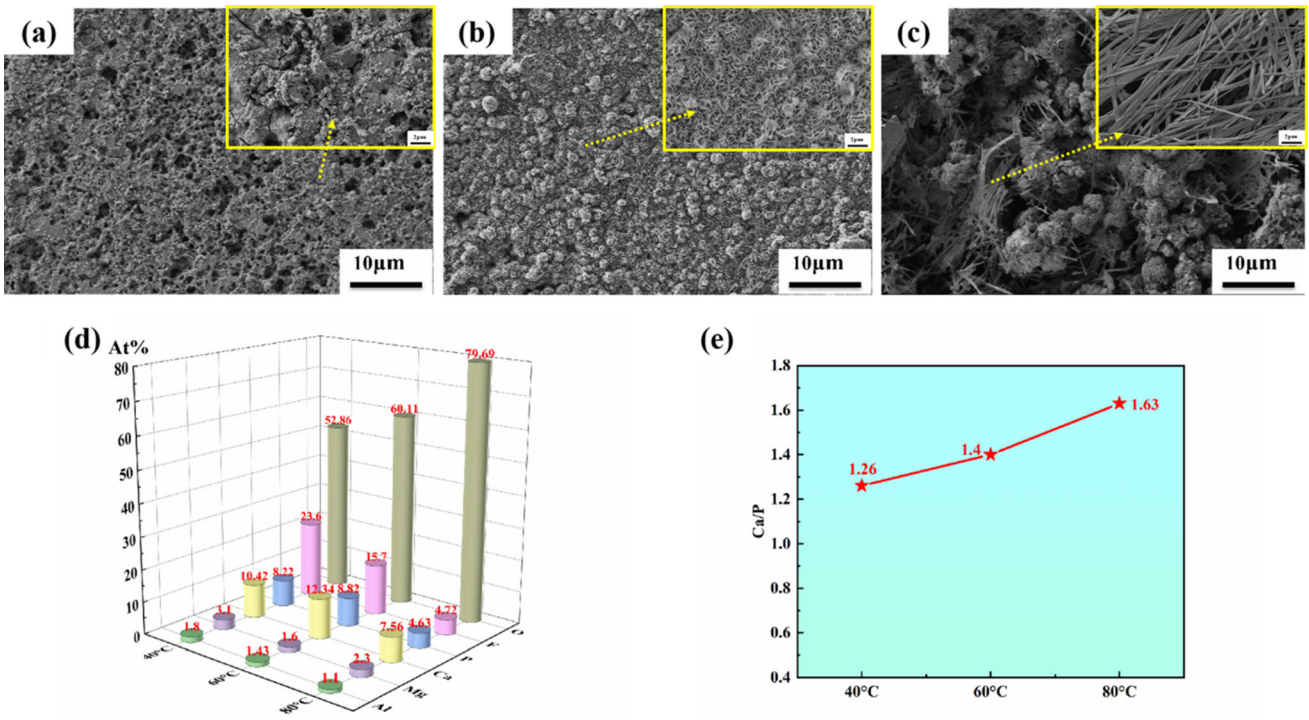

Fig. 1 The SEM surface morphologies of AZ31 Mg alloys coating F-CaP at (a) 40 °C, (b) 60 °C, (c) 80 °C and the the related (d) EDS components and (e) Ca/P ratio

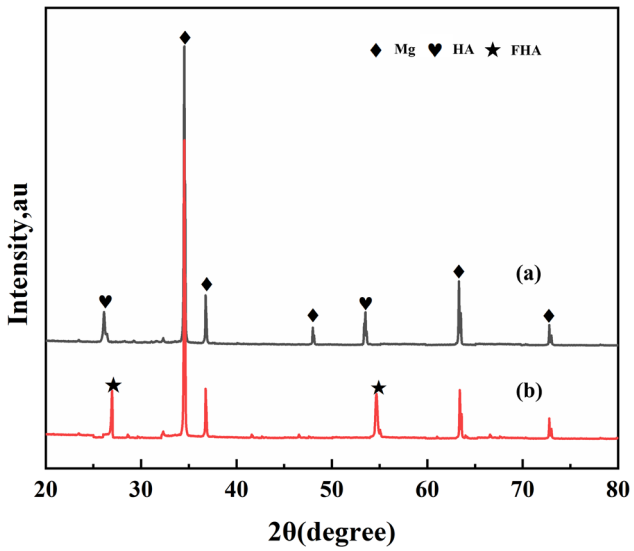

Fig. 2 X-ray diffraction patterns of (a) Ca-Ph coated AZ31 Mg alloys (b) F-CaP coated AZ31 Mg alloy at 80 °C

belong to the same main group; similar to Cl^-, F^- is also able to pass through the already formed coating. When NaF is added to the coating treatment solution, excessive F- passes through the coating, seriously destroys the previously formed coating, reacts with Mg(OH)2, and even directly corrodes the underlying matrix. The hydrogen bubbles caused by the corrosion matrix will occupy the F-CaP coating on the surface of the magnesium alloy, inhibiting the successful deposition of the F-CaP coating and further preventing the deposition of the complete FHA coating.

3.3 Evaluation of the Corrosion Behavior of F-CaP Coatings Synthesized at Different Temperatures

The influence of the fluoro-heat treatment temperature on the dynamic potential polarization curve of the obtained coating in SBF is shown in Figure 4. Table 1 displays the fitting findings of the curves acquired via Tafel extrapolation. The potentiodynamic polarization results showed that the corrosion resistance of the F-CaP coating was greater than that of the AZ31 substrate. The i_{corr} values of the bare substrate are significantly greater than those of all the coated alloys. As the fluorine heat treatment temperature increased, the corrosion potential (E_{corr}) increased from − 1.605 V at 40 °C to − 1.529 V at 60 °C, reaching − 1.412 V at 80 °C. Generally, the higher the corrosion potential is, the stronger the corrosion resistance of the sample, but the corrosion current density (i_{corr}) does not follow this rule. The corrosion current density at 60 °C is minimal, and the corrosion current density at 80 °C is less than that at 40 °C. However, it is still greater than that of the sample treated at 60 °C. This is because the corrosion potential can only be used as a thermodynamic parameter to describe the trend of corrosion resistance, and the density of corrosion currents is used to evaluate the corrosion rate. By calculating the rate of sample corrosion by Equation 1 (Ref 24), the corrosion rate of the produced coating sample is ∼ 0.101 mm/y at 60 °C, which is approximately 1/3 of the rate of corrosion of the addressed sample at 40 °C and 80 °C. This demonstrates that the corrosion resistance of the coating created at 60 °C is greater than that of the coatings applied at other temperatures.

Figure 5 shows the EIS impedance profiles of the bare and F-CaP coating samples prepared at different treatment temperatures. As shown in Figure 5(a), the diameter of the two arc responses can be seen in the Nyquist plots (Ref 25-28). The two arc responses correspond to two phase angle peaks in the Porter

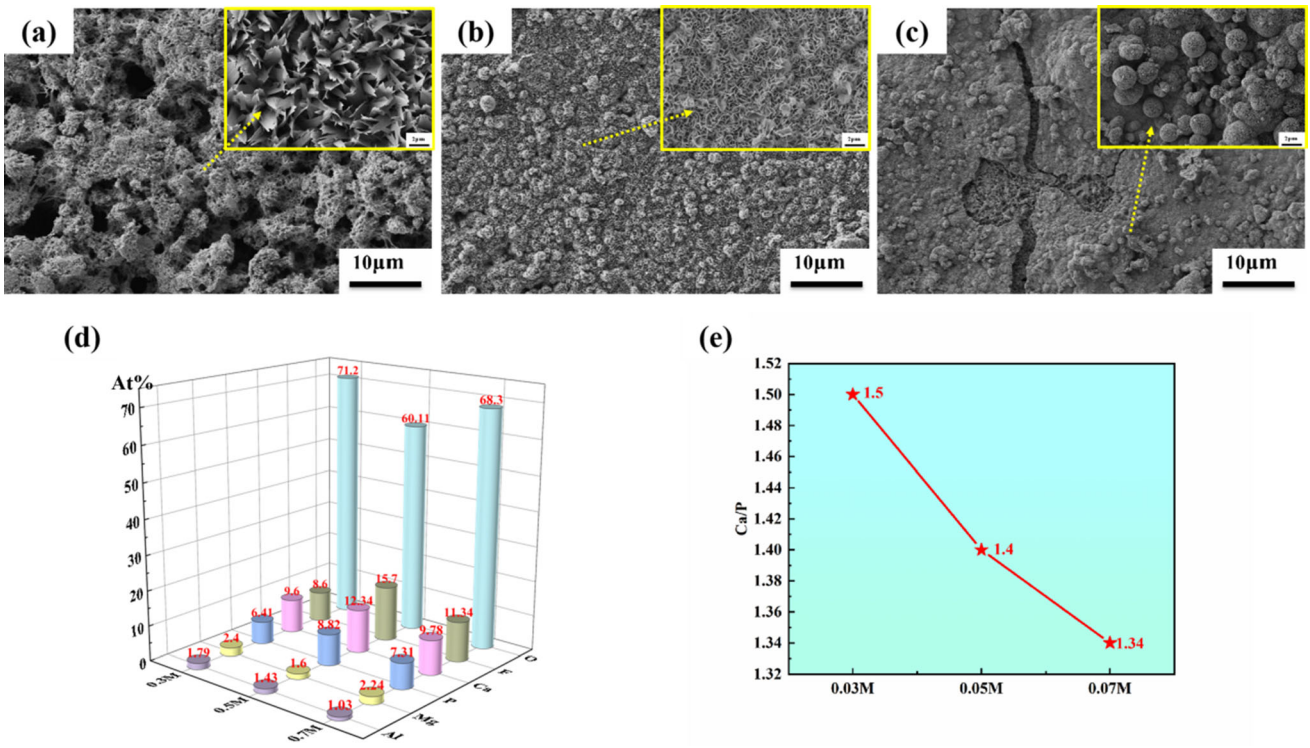

Fig. 3 The SEM surface morphologies of AZ31 Mg alloys coating F-CaP with different F^- addition (a) 0.3 M, (b) 0.5 M, (c) 0.7 M and the related (d) EDS components and (e) Ca/P ratio

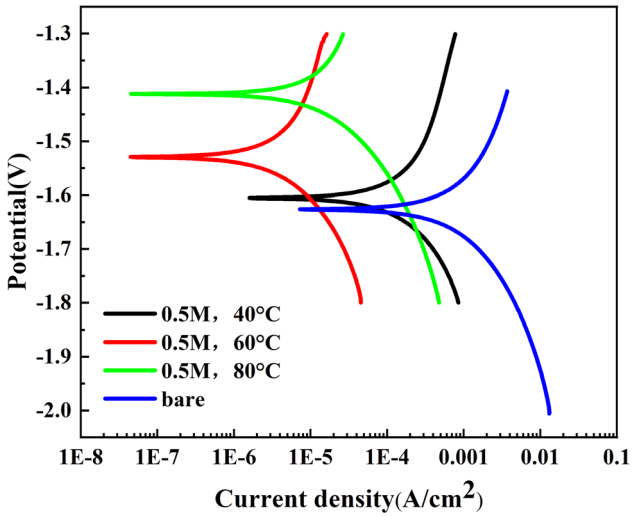

Fig. 4 Potentiodynamic polarization curves of bare and F-CaP coated AZ31 alloys obtained at different temperatures

Table 1 Corrosion parameters determined from the Tafel extrapolation method of Fig. 4

Sample	E_{corr}, V	i_{corr}, A/cm^2	P_i, mm/y
Bare	− 1.626	3.243×10^{-4}	7.409
0.5 M, 40 °C	− 1.605	1.651×10^{-5}	0.377
0.5 M, 60 °C	− 1.529	4.400×10^{-6}	0.101
05 M, 80 °C	− 1.412	1.468×10^{-5}	0.335

phase diagram, so two time constant elements are introduced when the equivalent circuit is fitted. As the treatment temperature increases, the impedance mode value increases and then decreases as shown in Figure 5(c), and the radius of the arc resistance also increases and then decreases. When the treatment temperature is 60 °C, the impedance mode value is the largest, and the radius of the arc resistance is also the largest. The F-CaP coating formed at 60 °C has the greatest ability to protect against the magnesium alloy structure in SBF solution and the strongest ability to protect against corrosive ion erosion. The equivalent circuit model of the AC impedance in SBF for the F-CaP coating prepared at different temperatures is shown in Figure 5(d). The fitted circuit elements R_s, Q_l, R_1, Q_2, and R_2 represent the solution resistance, the double-layer capacitance, the charge transfer resistance, and the coating capacitance and resistance, respectively. In the equivalent circuit model, the circuit (R_2, Q_2) is fitted according to the arc resistance in the high-frequency region in the Nyquist plots and the phase angle of the intermediate frequency range in the Porter phase diagram. The circuit (R_1, Q_1) corresponds to the arc resistance in the Nyquist plots in the low-frequency region (Ref 29). Table 2 shows the circuit fitting results, which indicate that the Rs solution resistance is very low, indicating that the solution resistance has little influence on the electrochemical test. All coatings had lower Q values than did the corrosion product films on the bare alloys. This indicates that the coating has fewer defects than the corrosion products formed on the bare alloy. The coating resistance and charge transfer resistance reach their maximum values at 60 °C, and the minimum Q value is caused by the minimum corrosion area (Ref 30, 31). Combined with SEM image analysis, the sample prepared at 60 °C has a small and dense scaly coating, and the

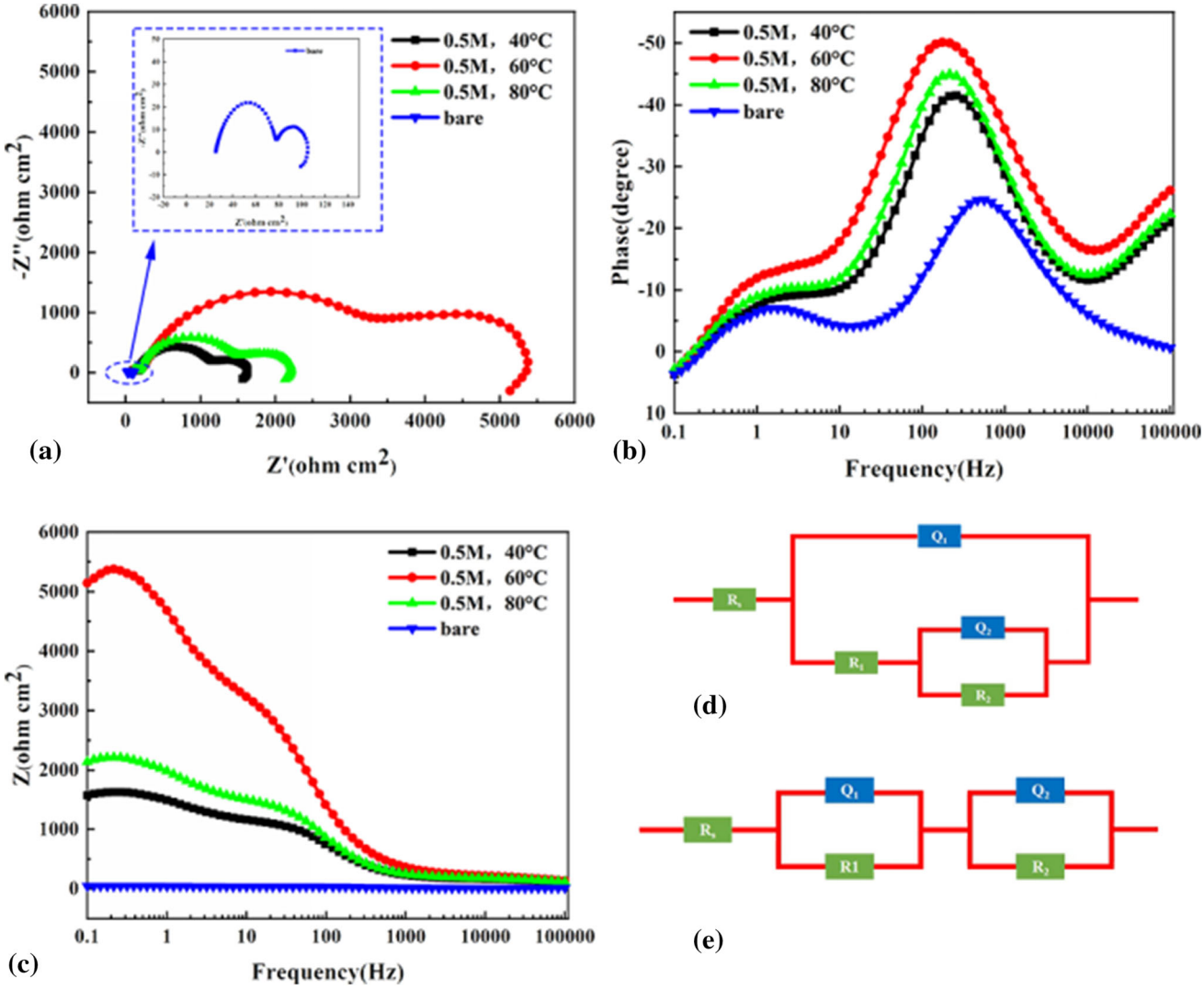

Fig. 5 EIS spectra of bare and F-CaP coated AZ31 Mg prepared at different temperatures (a) Nyquist plots, (b) Bode phase angle plots, (c) Magnitude plots, (d) equivalent circuit model of bare AZ31 Mg, and (e) equivalent circuit model of F-CaP coated AZ31 Mg for curve fitting of EIS results

Table 2 EIS fitting parameters of bare and F-CaP coated AZ31 Mg at different temperatures

Parameters	Bare	0.5 M, 40, °C	0.5 M, 60, °C	0.5 M, 80, °C
R_s (Ω cm^2)	25.74	58.06	81.20	73.20
Q_1 (S·s^n·cm^{-2})	2.94×10^{-5}	2.61×10^{-5}	2.116×10^{-6}	2.45×10^{-6}
n_1	0.853	0.8564	0.7247	0.6543
R_1 (Ω·cm^2)	54.24	759.3	2681	1013
Q_2 (S·s^n·cm^{-2})	4.292×10^{-3}	7.746×10^{-5}	2.218×10^{-6}	5.376×10^{-6}
n_2	1	0.7242	0.6589	0.8156
R_2 (Ω·cm^2)	23.18	200.3	4759	1897
χ^2	4.955×10^{-4}	6.314×10^{-4}	8.104×10^{-4}	7.572×10^{-4}

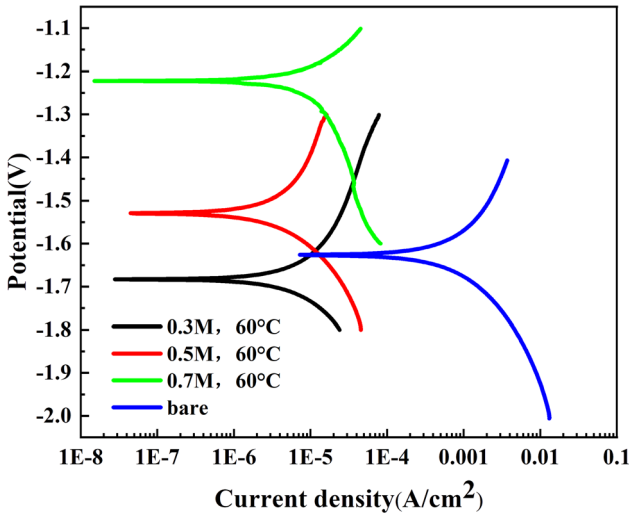

Fig. 6 Potentiodynamic polarization curves of Ca-Ph coatings with varying F^- content

dense coating structure effectively reduces the corrosion area. The corrosion resistance of the F-CaP membrane samples obtained by the 60 °C and 80 °C treatments improved, while the corrosion resistance decreased in the 40 °C sample. At 40 °C, the sample formed only loose and defective coatings. At 80 °C, the reaction temperature reached the formation barrier of FHA, which successfully generated smaller lattice parameters and a more compact crystal structure. FHA, which has a low solubility, greatly improved the corrosion resistance.

$$P_i = 22.85 i_{\text{corr}} \quad \text{(Eq 1)}$$

3.4 Evaluation of the Corrosion Behavior of F-CaP Coatings Synthesized with Different Fluoride Additions

Figure 6 shows the dynamic potential polarization curves of F-CaP coatings with different amounts of doped fluoride prepared at 60 °C. Table 3 shows the values for the equilibrium potential Ecorr, the density of corrosion currents icorr, and the corrosion rate Pi. The equilibrium potential of the 0.7 M coating was the highest, and the corrosion current density decreased and then increased with increasing fluoride content. The corrosion current density of the sample prepared by 0.5 M was the smallest, indicating that the corrosion rate of the coating prepared by 0.5 M in SBF was the smallest. This is related to the most compact structure of $S_{0.5\ M,\ 60\ °C}$ and the presence of visible holes in the $S_{0.3\ M,\ 60\ °C}$. When the coating preparation amount is 0.7 M, the excess F^- destroys the originally compact and intact coating, which cannot act as an effective physical barrier.

As shown in Figure 7(c), the low-frequency impedance modulus | Z | values of the 0.5 M fluoro-doped samples are significantly greater than the | Z | values of the other two doped samples. The modulus of low-frequency impedance increases with increasing corrosion resistance, so the coating sample with 0.5 M fluoride has the best corrosion resistance (Ref 23). Figure 7 shows the EIS impedance pattern of F-CaP coatings with different fluoride contents. According to the number of time constants of the two phase angles in the high-frequency region of the Nyquist plots combined with the port phase

Table 3 Corrosion parameters determined from the Tafel extrapolation method

Samples	E_{corr}, V	i_{corr}, A/cm^2	P_i, mm/y
Bare	− 1.626	3.243×10^{-4}	7.409
0.3 M, 60 °C	− 1.683	8.134×10^{-6}	0.185
0.5 M, 60 °C	− 1.529	4.400×10^{-6}	0.101
0.7 M, 60 °C	− 1.222	1.176×10^{-5}	0.269

diagram, the equivalent circuit input EIS data are shown in Figure 7(d). The fitted data are shown in Table 4. In addition, the sample with the 0.5 M film layer has the largest arc resistance diameter, which also indicates that the film layer can effectively enhance the corrosion resistance of the magnesium alloy. Figure 7(d) shows the equivalent circuit diagram of different fluorine-doped samples, where Rs is the solution resistance and R1 and Q1 are the charge transfer resistance and constant phase components, respectively. R_2 and Q_2 indicate the coating resistance and the coating capacitance, respectively. Usually, higher R values indicate lower corrosion rates (Ref 32, 33). Compared with 0.3 M and 0.7 M, 0.5 M had the highest resistance and charge transfer resistance, respectively, at 2681 Ω cm^2 and 4759 Ω cm^2, which acted as the best physical barrier, indicating that the membrane prepared under these conditions had better corrosion resistance.

3.5 The Corrosion Behavior of F-CaP Coated Samples During a Long-Term Immersion Test

To explore the degradation process of sample preparation under different conditions, the samples were soaked in SBF solution for 7 days. Hydrogen precipitation and weight loss are determined during the immersion process, and the corrosion rate is calculated. To ensure the accuracy of the immersion experiments, three repeated experiments were performed. As shown in Figure 8(a), the samples prepared at 60 °C show the lowest amount of hydrogen precipitation during the whole soaking process, and the curve is always the lowest. After 7 days of soaking, the volume of hydrogen released was only 5.289 mL/cm^2, which is 4/5 lower than that of the samples prepared under the other two conditions. The results of hydrogen analysis experiments show that the excellent stability of the sample coating prepared at 60 °C can provide effective protection for AZ31 magnesium alloys. Figure 4, 5, 6, 7, 8, 9 also shows that the samples treated at 60 °C have the highest corrosion resistance. Therefore, the hydrogen precipitation and sample weight loss can be arranged in the following increasing sequence: $S_{0.5\ M,\ 60\ °C} < S_{0.3\ M,\ 60\ °C} < S_{0.7\ M,\ 60\ °C} < S_{0.5\ M,\ 80\ °C} < S_{0.5\ M,\ 40\ °C}$. Figure 8(c) and 9(c) illustrates the predicted corrosion rates based on weight loss and hydrogen precipitation, which correspond well with the electrochemical measurements.

Figure 10 shows an illustration of the external structure of the samples after three and seven days in SBF solution. The surface morphology of the samples changes significantly with prolonged immersion time in SBF. Except for 0.5 M, the coating prepared at 40 °C exposed the underlying magnesium alloy matrix after soaking for 7 days, and the surfaces of the other samples were covered. After 3 days of $0.S_{5\ M,\ 60\ °C}$ F-CaP coating covers the samples, and the surface-scale crystals turn into whiskers, indicating that Ca^{2+} and PO_4^{3-} in SBF are

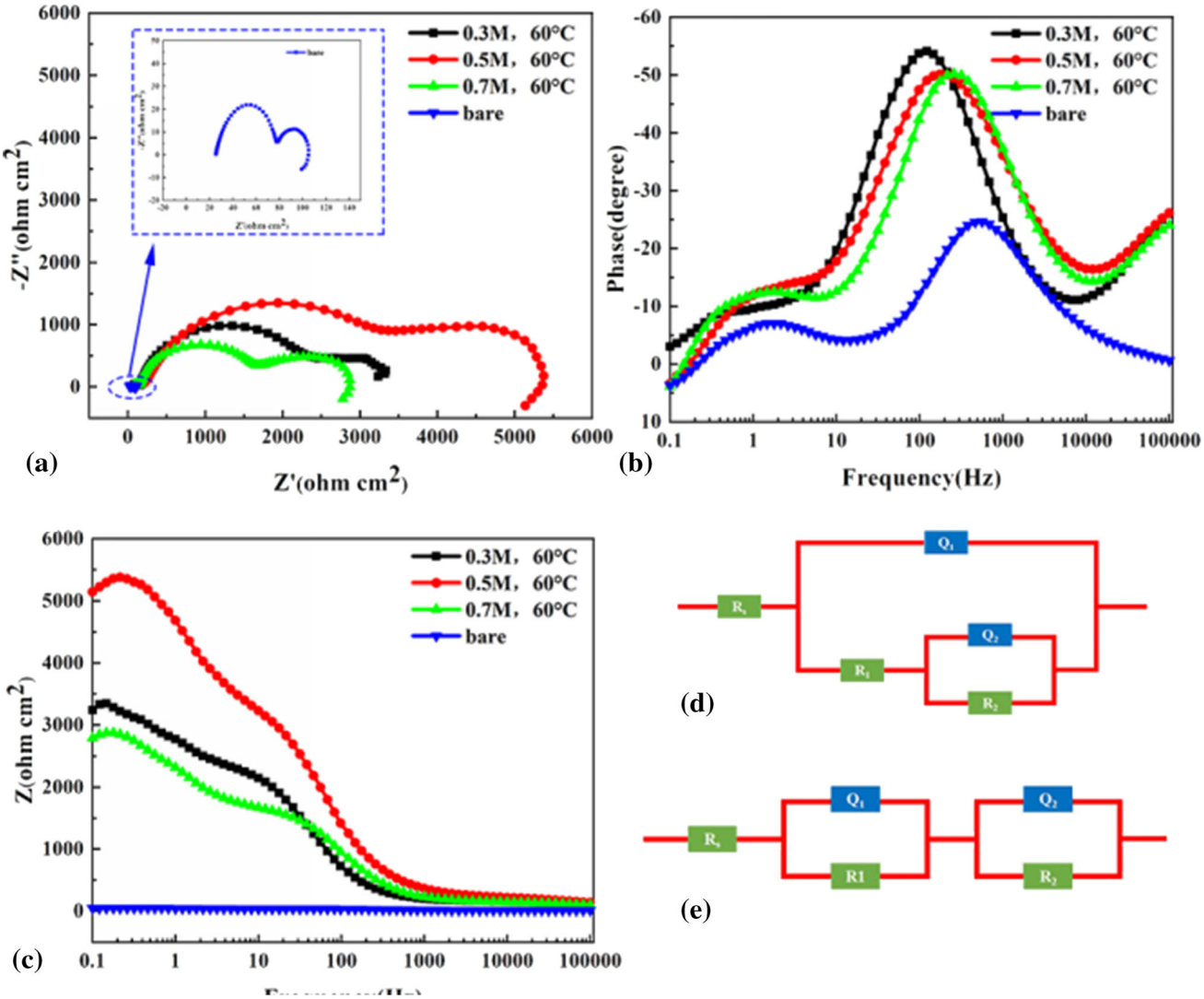

Fig. 7 EIS spectra of F-CaP coatings prepared with different F- content (a) Nyquist plots, (b) Bode phase angle plots, (c) Magnitude plots, (d) equivalent circuit model of bare AZ31 Mg, and (e) equivalent circuit model of F-CaP coated AZ31 Mg for curve fitting of EIS results

Table 4 EIS fitting parameters of AZ31 Mg alloys coating F-CaP with varying F^- content

Parameters	Bare	0.3 M, 60 °C	0.5 M, 60 °C	0.7 M, 60 °C
R_s ($\Omega \cdot cm^2$)	25.74	55.18	81.20	79.70
Q_1 ($S \cdot s^n \cdot cm^{-2}$)	2.94×10^{-5}	8.866×10^{-6}	2.116×10^{-6}	2.84×10^{-6}
n_1	0.853	0.9069	0.7247	0.6730
R_1 ($\Omega \cdot cm^2$)	54.24	1963	2681	1409
Q_2 ($S \cdot s^n \cdot cm^{-2}$)	4.292×10^{-3}	6.649×10^{-6}	2.218×10^{-6}	2.146×10^{-6}
n_2	1	0.8371	0.6589	0.7542
R_2 ($\Omega \cdot cm^2$)	23.18	2778	4759	2055
χ^2	4.955×10^{-4}	7.243×10^{-4}	8.104×10^{-4}	9.527×10^{-4}

dissolved and regenerated on the surface of HA. After 7 days, the surface has no obvious damage, the protective layer remains complete and thick, and the agglomeration becomes spherical HA, which retains its good corrosion resistance. However, in the samples prepared under other conditions, the massive formation of cracks and corrosion layers cause the film layer to crack and stratify, and the film layer lowers the sample's corrosion resistance even further and increases its disintegration rate (Ref 30).

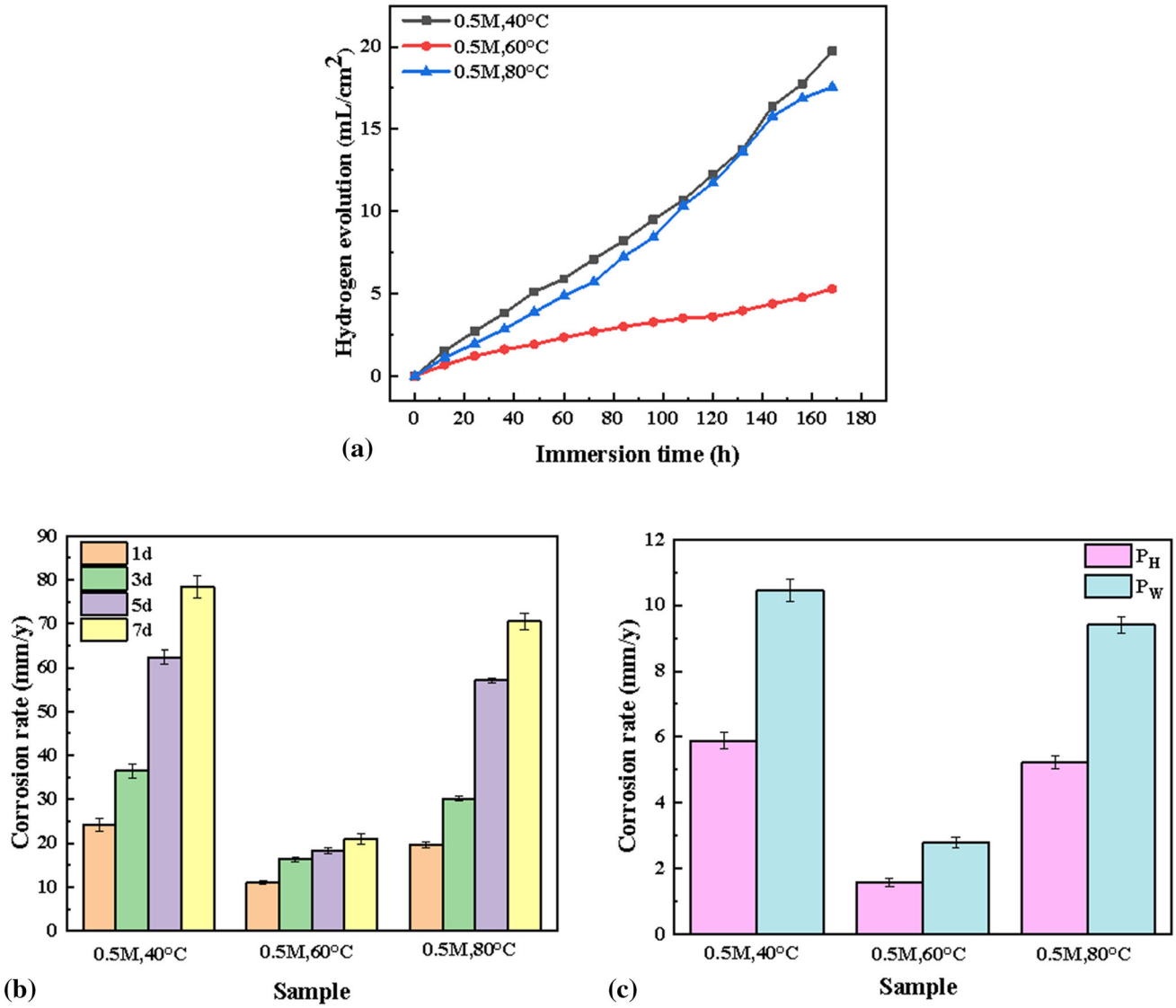

Fig. 8 Immersion test results of AZ31 Mg alloys coating F-CaP at various temperatures: (a) volume change of Hydrogen evolution, (b) coating weight loss as a function of SBF solution exposure time and (c) corrosion rate comparison after 7 days

4. Conclusions

By changing the temperature and amount of F^- added, different F-CaP coatings were prepared on the magnesium alloy. The sample morphology and content were investigated by different characterization methods, and the electrochemical properties and in vitro degradation behavior were studied by electrochemical tests and soaking experiments. The following conclusions were obtained:

1. Temperature had a great effect on the morphology of the F-CaP coating. An increase in the temperature accelerates the reaction rate of the ions during the deposition process, creating a compact and dense coating and promoting the generation of the FHA phase. However, when the temperature is too high, the violent reaction produces a large amount of hydrogen, which occupies the growth position of the coating so that some positions cannot be covered by the coating and produces an impact force when ruptured, prompting the formed coating to fall off and dissolve.
2. When the amount of fluoride ions is insufficient, the F-CaP coating cannot completely cover the surface of the matrix. If the amount of fluoride is too large, excessive fluoride ions will pass through the surface of the uncoated coating and react with the matrix, hindering the growth of the F-CaP coating.

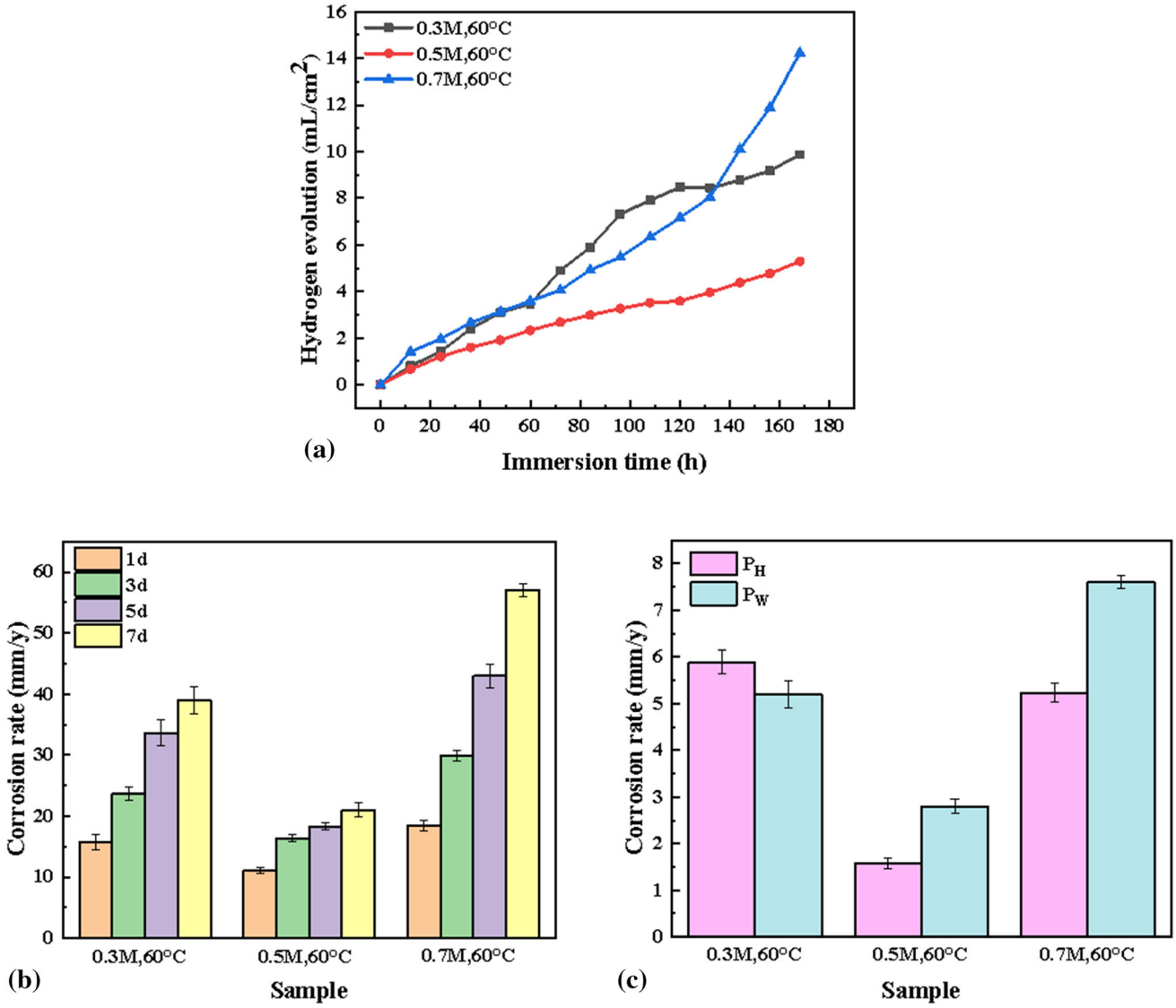

Fig. 9 Immersion test results of AZ31 Mg alloys coating F-CaP with varying F^- content: (a) volume change of Hydrogen evolution, (b) coating weight loss as a function of SBF solution exposure time and (c) corrosion rate comparison after 7 days

3. The full and compact coating morphology efficiently shields AZ31 magnesium alloy against corrosion by simulated bodily fluids when the concentration of doped fluorine ions is 0.5 M and the temperature is adjusted to 60 °C.

Acknowledgment

This work was supported by the National Natural Science Foundations of China [Grant Numbers 52374395 and 52122408]; the Natural Science Foundation of Shanxi province [Grant Numbers 20210302123163]; the Central Government Guided

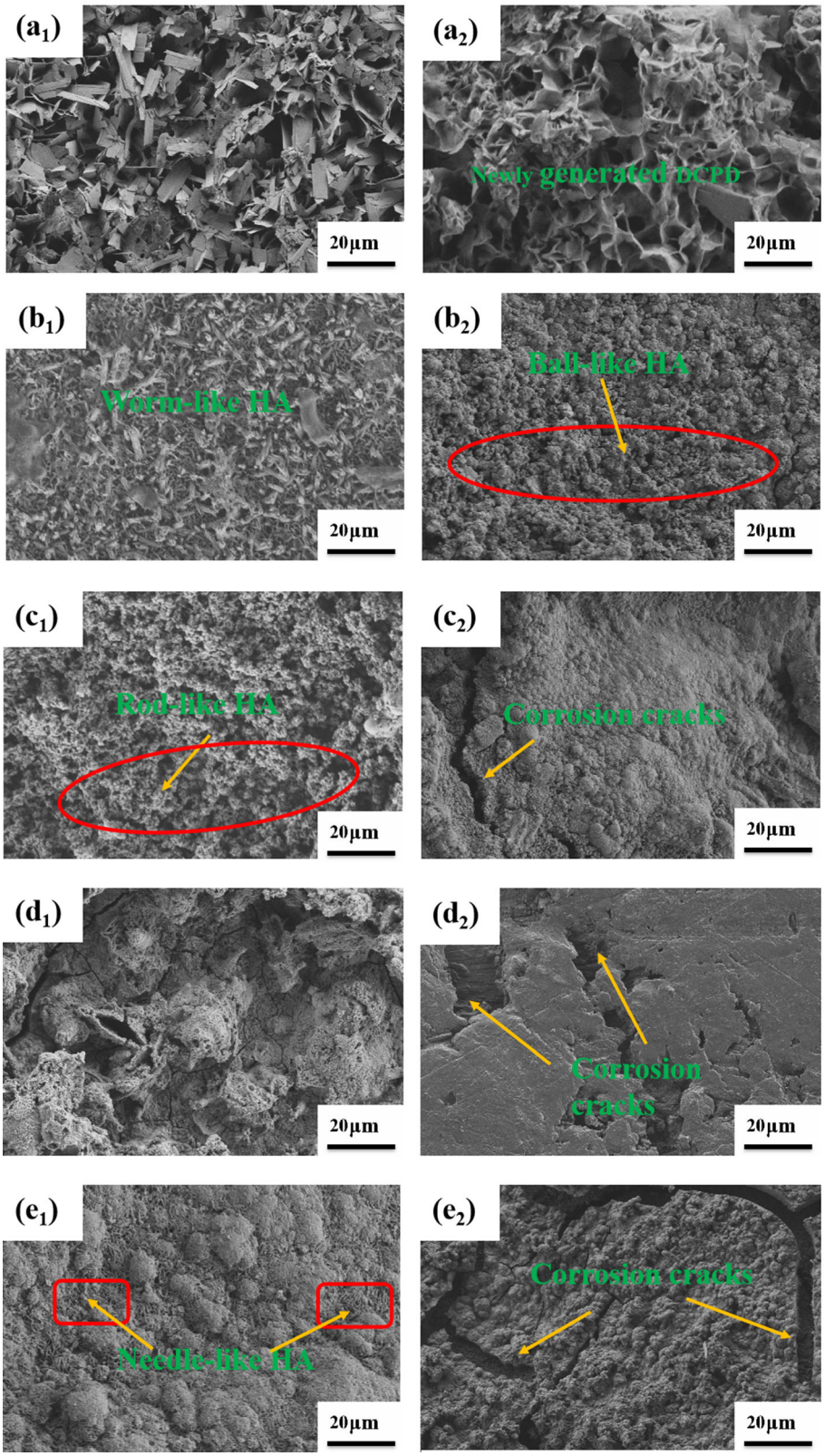

Fig. 10 Surface morphologies of the sample handled at 0.3 M,60 °C (a_1 and a_2), 0.5 M, 60 °C (b_1 and b_2),0.7 M, 60 °C (c_1 and c_2), 0.5 M, 40 °C (d_1 and d_2) ,0.5 M, 80 °C (e_1 and e_2) immersed in SBF for 3 days (a_1, b_1, c_1, d_1 and e_1) and 7 days (a_2, b_2, c_2, d_2 and e_2)

Local Science and Technology development projects [Grant Numbers YDZJSX2021A010]; the China Postdoctoral Science Foundation [Grant Numbers 2022M710541]; the Research Project Supported by Shanxi Scholarship Council of China [Grant Numbers 2022-038]; the Ministry of Science and Higher Education of the Russian Federation for financial support under the Mega-

grant [Grant Numbers 075-15-2022-1133], the National Research Foundation (NRF) grant funded by the Ministry of Science and ICT [Grant Numbers 2015R1A2A1A01006795] of Korea through the Research Institute of Advanced Materials, National Key Research and Development Program of China (No. 2021YFB3701100), Key Research and Development, Plan of Shanxi Province [No. 202102050201005], Applied Basic Research Program Project of Liaoning Province of China (No.2023020253-JH2/1016).

Author contributions

Liuwei Zheng contributed to investigation, writing—original draft, conceptualization. Lifei Wang contributed to methodology, conceptualization, writing—review and editing, supervision. Hua Chai contributed to data curation. Chaoyang Yang contributed to formal analysis. Zhipeng Ge contributed to software. Hongxia Wang contributed to funding acquisition. Weili Cheng contributed to data curation. Hua Zhang contributed to visualization. Fugang Qi contributed to investigation. Xiaoye Zhou contributed to methodology. Hanuma Reddy Tiyyagura contributed to resources. Kwang Seon Shin contributed to resources, writing—review and editing.

Data availability

The authors do not have permission to share data.

Conflict of interest

The authors declare that they have no known competing financial interests or personal relationships that could have appeared to influence the work reported in this paper.

References

1. F. Witte, J. Fischer, J. Nellesen, H.-A. Crostack, V. Kaese, A. Pisch, F. Beckmann, and H. Windhagen, In Vitro and In Vivo Corrosion Measurements of Magnesium Alloys, *Biomaterials*, 2006, **27**(7), p 1013–1018. https://doi.org/10.1016/j.biomaterials.2005.07.037
2. L. Xu, G. Yu, E. Zhang, F. Pan, and K. Yang, In Vivo Corrosion Behavior of Mg-Mn-Zn Alloy for Bone Implant Application, *J. Biomed. Mater. Res. Part A*, 2010, **83A**(3), p 703–711. https://doi.org/10.1002/jbm.a.31273
3. Y.F. Zheng, X.N. Gu, and F. Witte, Biodegradable Metals, *Mater. Sci. Eng. R. Rep.*, 2014, **77**, p 1–34. https://doi.org/10.1016/j.mser.2014.01.001
4. M.P. Staiger, A.M. Pietak, J. Huadmai, and G. Dias, Magnesium and Its Alloys as Orthopedic Biomaterials: A Review, *Biomaterials*, 2006, **27**(9), p 1728–1734. https://doi.org/10.1016/j.biomaterials.2005.10.003
5. T. Kraus, S.F. Fischerauer, A.C. Hänzi, P.J. Uggowitzer, J.F. Löffler, and A.M. Weinberg, Magnesium Alloys for Temporary Implants in Osteosynthesis: In vivo Studies of their Degradation and Interaction with Bone, *Acta Biomater.*, 2012, **8**(3), p 1230–1238. https://doi.org/10.1016/j.actbio.2011.11.008
6. X.B. Chen, D.R. Nisbet, R.W. Li, P.N. Smith, T.B. Abbott, M.A. Easton, D.H. Zhang, and N. Birbilis, Controlling Initial Biodegradation of Magnesium by a Biocompatible Strontium Phosphate Conversion Coating, *Acta Biomater.*, 2014, **10**(3), p 1463–1474. https://doi.org/10.1016/j.actbio.2013.11.016
7. J. Yang, X. Lu, C. Blawert, S. Di, and M.L. Zheludkevich, Microstructure and Corrosion Behavior of Ca/P Coatings Prepared on Magnesium by Plasma Electrolytic Oxidation, *Surf. Coat. Technol.*, 2017, **319**, p 359–369. https://doi.org/10.1016/j.surfcoat.2017.04.001
8. Y. Song, S. Zhang, J. Li, C. Zhao, and X. Zhang, Electrodeposition of Ca-P Coatings on Biodegradable Mg Alloy: In Vitro Biomineralization Behavior, *Acta Biomater.*, 2010, **6**(5), p 1736–1742. https://doi.org/10.1016/j.actbio.2009.12.020
9. J. Wang, Y. Chao, Q. Wan, Z. Zhu, and H. Yu, Fluoridated Hydroxyapatite Coatings on Titanium Obtained by Electrochemical Deposition, *Acta Biomater.*, 2009, **5**(5), p 1798–1807. https://doi.org/10.1016/j.actbio.2009.01.005
10. Y. Huang, Y. Yan, and X. Pang, Electrolytic Deposition of Fluorine-Doped Hydroxyapatite/ZrO2 Films on Titanium for Biomedical Applications, *Ceram. Int.*, 2013, **39**(1), p 245–253. https://doi.org/10.1016/j.ceramint.2012.06.017
11. B.D. Hahn, Y.L. Cho, D.S. Park, J.J. Choi, J. Ryu, J.W. Kim, C.W. Ahn, C. Park, H.E. Kim, and S.G. Kim, Effect of Fluorine Addition on the Biological Performance of Hydroxyapatite Coatings on Ti by Aerosol Deposition, *J. Biomater. Appl.*, 2013, **27**, p 587–594. https://doi.org/10.1177/0885328211415572
12. E.C. Meng, S.K. Guan, H.X. Wang, L.G. Wang, S.J. Zhu, J.H. Hu, C.X. Ren, J.H. Gao, and Y.S. Feng, Effect of Electrodeposition Modes on Surface Characteristics and Corrosion Properties of Fluorine-Doped Hydroxyapatite Coatings on Mg-Zn-Ca Alloy, *Appl. Surf. Sci.*, 2011, **257**(11), p 4811–4816. https://doi.org/10.1016/j.apsusc.2010.12.073
13. H.R. Bakhsheshi-Rad, E. Hamzah, M. Daroonparvar, M.A.M. Yajid, M. Kasiri-Asgarani, M.R. Abdul-Kadir, and M. Medraj, In-Vitro Degradation Behavior of Mg Alloy Coated by Fluorine Doped Hydroxyapatite and Calcium Deficient Hydroxyapatite, *Trans. Nonferrous Metals Soc. China*, 2014, **24**(8), p 2516–2528. https://doi.org/10.1016/S1003-6326(14)63378-1
14. E.C. Moreno, M. Kresak, and R.T. Zahradnik, Fluoridated Hydroxyapatite Solubility and Caries Formation, *Nature*, 1974, **247**, p 64–65. https://doi.org/10.1038/247064a0
15. Z.J. Jia, M. Li, Q. Liu, X.C. Xu, Y. Cheng, Y.F. Zheng, T.F. Xi, and S.C. Wei, Micro-arc Oxidization of a Novel Mg-1Ca Alloy in Three Alkaline KF Electrolytes: Corrosion Resistance and Cytotoxicity, *Appl. Surf. Sci.*, 2014, **292**, p 1030–1039. https://doi.org/10.1016/j.apsusc.2013.11.038
16. E.A. Abdel-Aal, D. Dietrich, S. Steinhaeuser, and B. Wielage, Electrocrystallization of Nanocrystallite Calcium Phosphate Coatings on Titanium Substrate at Different Current Densities, *Surf. Coat. Technol.*, 2008, **202**(24), p 5895–5900. https://doi.org/10.1016/j.surfcoat.2008.06.139
17. C. Prakash and M.S. Uddin, Surface Modification of β-Phase Ti Implant by Hydroaxyapatite Mixed Electric Discharge Machining to Enhance the Corrosion Resistance and In-Vitro Bioactivity, *Surf. Coat. Technol.*, 2017, **326**, p 134–145. https://doi.org/10.1016/j.surfcoat.2017.07.040
18. M. Tomozawa and S. Hiromoto, Growth Mechanism of Hydroxyapatite-Coatings Formed on Pure Magnesium and Corrosion Behavior of the Coated Magnesium, *Appl. Surf. Sci.*, 2011, **257**(19), p 8253–8257. https://doi.org/10.1016/j.apsusc.2011.04.087
19. J. Han, B. Luthringer, S. Tang, J. Hu, C. Blawert, and M.L. Zheludkevich, Evolution and Performance of a MgO/HA/DCPD Gradient Coating on Pure Magnesium, *J. Alloy. Compd.*, 2021, **883**, 160793. https://doi.org/10.1016/j.jallcom.2021.160793
20. N. Aboudzadeh, C. Dehghanian, and M.A. Shokrgozar, Effect of Electrodeposition Parameters and Substrate on Morphology of Si-HA Coating, *Surf. Coat. Technol.*, 2019, **375**, p 341–351. https://doi.org/10.1016/j.surfcoat.2019.07.016
21. M. Tomozawa and S. Hiromoto, Microstructure of Hydroxyapatite- and Octacalcium Phosphate-Coatings Formed on Magnesium by a Hydrothermal Treatment at Various pH Values, *Acta Mater.*, 2011, **59**(1), p 355–363. https://doi.org/10.1016/j.actamat.2010.09.041
22. C. Wang, K.-Z. Li, Y.-Q. Zhai, H.-J. Li, J.-L. Wang, and G.-S. Jiao, Study of Fluorhydroxyapatite Coatings on Carbon/Carbon Composites, *Surf. Coat. Technol.*, 2009, **203**(13), p 1771–1775. https://doi.org/10.1016/j.surfcoat.2008.12.009
23. X. Wang, Y. Zhou, L. Xia, C. Zhao, L. Chen, D. Yi, J. Chang, L. Huang, X. Zheng, H. Zhu, Y. Xie, Y. Xu, and K. Lin, Fabrication of Nano-Structured Calcium Silicate Coatings with Enhanced Stability, Bioactivity and Osteogenic and Angiogenic Activity, *Colloids Surf. B*, 2015, **126**, p 358–366. https://doi.org/10.1016/j.colsurfb.2014.11.044
24. H.R. Bakhsheshi-Rad, M.H. Idris, M.R. Abdul-Kadir, A. Ourdjini, M. Medraj, M. Daroonparvar, and E. Hamzah, Mechanical and Bio-Corrosion Properties of Quaternary Mg-Ca-Mn-Zn Alloys Compared

with Binary Mg-Ca Alloys, *Mater. Des.*, 2014, **53**, p 283–292. https://doi.org/10.1016/j.matdes.2013.06.055
25. Y. Ouyang, Z. Chen, C. Jiang, W. Yang, Y. Chen, X. Yin, and Y. Liu, Design of the Double-Layer Biocompatible Coating on AZ31 Magnesium Alloy for Highly Effective Corrosion Resistance, *Surf. Coat. Technol.*, 2021, **428**, 127897. https://doi.org/10.1016/j.surfcoat.2021.127897
26. Y. Guo, Y. Su, R. Gu, Z. Zhang, G. Li, J. Lian, and L. Ren, Enhanced Corrosion Resistance and Biocompatibility of Biodegradable Magnesium Alloy Modified by Calcium Phosphate/Collagen Coating, *Surf. Coat. Technol.*, 2020, **401**, 126318. https://doi.org/10.1016/j.surfcoat.2020.126318
27. M. Tomozawa, S. Hiromoto, and Y. Harada, Microstructure of Hydroxyapatite-Coated Magnesium Prepared in Aqueous Solution, *Surf. Coat. Technol.*, 2010, **204**(20), p 3243–3247. https://doi.org/10.1016/j.surfcoat.2010.03.023
28. J.E. Gray-Munro and M. Strong, The Mechanism of Deposition of Calcium Phosphate Coatings from Solution Onto Magnesium Alloy AZ31, *J. Biomed. Mater. Res. Part A*, 2009, **90**(2), p 339–350. https://doi.org/10.1002/jbm.a.32107
29. H.R. Bakhsheshi-Rad, E. Hamzah, M. Daroonparvar, M.A.M. Yajid, and M. Medraj, Fabrication and Corrosion Behavior of Si/HA Nano-Composite Coatings on Biodegradable Mg-Zn-Mn-Ca Alloy, *Surf. Coat. Technol.*, 2014, **258**, p 1090–1099. https://doi.org/10.1016/j.surfcoat.2014.07.025
30. Y. Cai, S. Zhang, X. Zeng, M. Qian, D. Sun, and W. Weng, Interfacial Study of Magnesium-Containing Fluoridated Hydroxyapatite Coatings, *Thin Solid Films*, 2011, **519**(15), p 4629–4633. https://doi.org/10.1016/j.tsf.2011.01.007
31. M. Metikoš-Huković, R. Babić, Z. Grubač, M. Petravić, and R. Peter, Potential Assisted Formation and Characterization of Hydroxyapatite Coatings on Biodegradable Magnesium Alloys, *J. Electrochem. Soc.*, 2013, **160**(10), p 674–680. https://doi.org/10.1149/2.021310jes
32. S. Mallakpour, M. Khani, F. Mallakpour, and M. Fathi, Production of Polyvinylpyrrolidone/Chiral Diacid Modified Nanocrystalline Mg-Substituted Fluorapatite Nanocomposites: Morphological and Thermal Characterization, *J. Appl. Polym. Sci.*, 2016 https://doi.org/10.1002/app.44254
33. T.A. Aljohani, S. Aljadaan, M.T. Bin Rubayan, and F. Khoshnaw, Impact of Processing Parameters in Plasma Electrolytic Oxidation on Corrosion Resistance of Magnesium Alloy Type AZ91, *Eng. Rep.*, 2022, **4**(2), p e12459. https://doi.org/10.1002/eng2.12459